

1 **Droplet collection efficiencies inferred from satellite retrievals**
2 **constrain effective radiative forcing of aerosol-cloud interactions**

3 Charlotte M. Beall¹, Po-Lun Ma¹, Matthew W. Christensen¹, Johannes Mülmenstädt¹, Adam
4 Varble¹, Kentaroh Suzuki², Takuro Michibata³

5 ¹Atmospheric Sciences and Global Change Division, Pacific Northwest National Laboratory, Richland, WA, 99354,
6 U.S.A.

7 ²Atmosphere and Ocean Research Institute, University of Tokyo, Chiba, 277-8568, Japan

8 ³Department of Earth Science, Okayama University, Okayama, 700-8530, Japan

9 *Correspondence to:* Charlotte M. Beall; charlotte.beall@pnnl.gov

10

11 **Abstract.** Process-oriented observational constraints for the anthropogenic effective radiative forcing due to aerosol-
12 cloud-interactions (ERF_{aci}) are highly desirable because the uncertainty associated with ERF_{aci} poses a significant
13 challenge to climate prediction. The Contoured Frequency by Optical Depth Diagrams (CFODD) analysis supports
14 evaluation of model representation of cloud liquid to rain conversion processes because the slope of a CFODD,
15 generated from joint MODerate Resolution Imaging Spectroradiometer (MODIS)-CloudSat cloud retrievals, provides
16 an estimate of cloud droplet collection efficiency in single-layer warm liquid clouds. Here we present an updated
17 CFODD analysis as an observational constraint for the ERF_{aci} due to warm rain processes and apply it to the U.S.
18 Department of Energy's Energy Exascale Earth System Model version 2 (E3SMv2). A series of sensitivity
19 experiments shows that E3SMv2 droplet collection efficiencies and ERF_{aci} are highly sensitive to autoconversion,
20 the rate of mass transfer from cloud liquid to rain, yielding a strong correlation between the CFODD slope and the
21 shortwave component of ERF_{aci} (ERF_{aci,sw}; Pearson's R = -0.91). E3SMv2's CFODD slope (0.20 ± 0.04) is in
22 agreement with observations (0.20 ± 0.03). The strong sensitivity of ERF_{aci,sw} to the CFODD slope provides a useful
23 constraint on highly uncertain warm rain processes, wherebyWe estimate ERF_{aci,sw}, constrained by MODIS-
24 CloudSat, is estimated by calculating the intercept of the linear association between the ERF_{aci,sw} and the CFODD
25 slopes, using the MODIS-CloudSat CFODD slope as a reference. When E3SMv2's CFODD slope is constrained to
26 agree with the A-Train retrievals, ERF_{aci,sw} is reduced by $14 \pm 6\%$ in magnitude, indicating that correcting bias in the
27 ERF_{aci,sw} due to autoconversion would bring E3SMv2's total ERF_{aci} (-1.50 W m^{-2}) into better agreement with the
28 IPCC AR6 'very likely' range for ERF_{aci} ($-1.0 \pm 0.7 \text{ W m}^{-2}$).

29

30 **1 Introduction**

Formatted: Subscript

31 Single-layer, low-level marine warm clouds cover 25% of the ocean surface (Charlson et al., 1987) and exert a strong
32 cooling effect on climate due to their reflectivity (Hartmann et al., 1992; Hartmann and Short, 1980; Ramanathan et
33 al., 1989). Aerosols modulate multiple radiative properties of low warm clouds, including droplet number
34 concentration (N_d), liquid water path (LWP), geometric , cloud fraction, and lifetime, and their net impact on the cloud
35 radiative forcing is the most uncertain component of the climate system (e.g., Stevens and Feingold, 2009;
36 Christensen et al., 2020; Glassmeier et al., 2021). Though aerosols also exert a significant influence on ice and mixed-
37 phase clouds, aerosol-cloud interactions (ACI) make their largest contribution to global radiative forcing via liquid
38 water clouds (Bellouin et al., 2020).

39 In marine warm cloud regimes, an increase in aerosol concentrations typically leads to increasing N_d . Given constant
40 condensed water content, enhanced aerosol concentrations increase cloud albedo due to higher concentrations of
41 smaller cloud droplets through the so-called “Twomey effect” (Twomey, 1974). However, the cooling effect of
42 increased N_d can be offset or enhanced by competing aerosol-mediated cloud properties such as cloud fraction and
43 LWP. For example, increased numbers of smaller droplets can diminish cloud fraction by reducing cloud droplet
44 sedimentation (Bretherton et al., 2007) and increasing cloud-top evaporation and dry air entrainment (Wang et al.,
45 2003). On the other hand, aerosols can also increase cloud fraction and vertical extent by suppressing precipitation
46 (Albrecht, 1989; Pincus and Baker, 1994). Christensen et al. (2020) demonstrated that the impact of aerosol on low-
47 level cloud areal coverage depends on the stability of the atmosphere: in thermodynamically stable lower tropospheric
48 conditions, increased aerosol results in increased cloud fraction, lifetime and N_d , whereas in unstable conditions,
49 entrainment and evaporation offset Twomey effects, resulting in relatively smaller changes to cloud radiative
50 properties.

51 Earth Systems Models (ESMs) are relied upon for estimating the global Effective Radiative Forcing of Aerosol-Cloud
52 Interactions (ERFaci) due to the dearth of observations from the pre-industrial era. Yet ESM estimates are challenged
53 by the lack of observational constraints on ERFaci and the cloud processes that modulate ERFaci, which must be
54 parameterized due to the computational expense of explicitly resolving them. Mülmenstädt et al. (2020) proposed a
55 renewed focus on process-oriented observational constraints as a solution to “equifinality”, whereby differing
56 representations of cloud processes can reproduce observed state variables such as LWP and cloud fraction. The
57 problem of equifinality renders many global long-term observations of state variables useless for constraining ERFaci

58 on their own. Mülmenstädt et al. (2020) argues that constraints based on cloud process observations are thus highly
59 desirable as an alternative approach to state variable-based constraints because mitigating bias in a cloud process
60 representation will improve estimates of the response of the process to aerosols. Process-oriented constraints on
61 ERFaci are useful for quantifying the sensitivity of ERFaci to a specific process or constraining the component of
62 ERFaci that is affected by a process, rather than for constraining ERFaci overall (Mülmenstädt and Feingold, 2018).
63 Recent examples of process-based diagnostics include the Earth System Model Aerosol-Cloud Diagnostics Package
64 (ESMAC Diags) (Tang et al., 2022; Tang et al., 2023), which supports evaluation of aerosol activation processes, and
65 Varble et al. (2023) which demonstrated multiple model-observations comparison approaches that target processes
66 affecting cloud albedo susceptibility using geostationary satellite data and surface-based observations. Christensen et
67 al. (2023) applied ground-based measurements, satellite retrievals and meteorological reanalysis products in a
68 Lagrangian framework to evaluate multiple aerosol-cloud processes in E3SM, including cloud condensation nuclei
69 deposition via precipitation and the temporal response in N_d to aerosol perturbations.

70 In response to the demand for process-oriented constraints on warm liquid cloud processes, we present a constraint on
71 the shortwave component of ERFaci (ERFaci_{sw}) due to autoconversion, a parameterization representing the transfer
72 of liquid mass and number from the cloud to rain category, based on satellite cloud retrievals. For the past 12 years,
73 prior studies have applied the Contoured Frequency by Optical Depth Diagrams (CFODD) analysis (Nakajima et al.
74 2010; Suzuki et al. 2010) to evaluate model representation of warm rain processes because the slopes of CFODDs,
75 generated from spaceborne radar reflectivity profiles (CloudSat) (e.g. Marchand et al., 2008) and cloud property
76 retrievals from the Moderate Resolution Imaging Spectroradiometer (MODIS) (e.g. Platnick et al., 2017), provide an
77 estimate of cloud droplet collection efficiency in warm liquid clouds (Suzuki et al. 2010). Here we demonstrate how
78 an updated CFODD analysis can be applied to constrain ERFaci due to autoconversion using the U.S. Department of
79 Energy's Energy Exascale Earth System Model version 2 (E3SMv2) and the relationship between CFODD slopes and
80 ERFaci_{sw} in SLWCs.

81 To support the application of CFODD analysis as a constraint on ERFaci_{sw}, we modified the Warm Rain Diagnostics
82 (WRDs) subroutine (Michibata et al. 2019) that was recently implemented in the Cloud Feedback Model
83 Intercomparison Project (CFMIP) Observations Simulator Package (COSPV2.0), a software package that supports
84 climate model evaluation against satellite observations (Michibata et al., 2019; Swales et al., 2018). The WRDs

85 support evaluation of model warm rain processes in single-layer warm liquid clouds (SLWCs) based on joint statistics
86 from MODIS and CloudSat. The first diagnostic provides the fractional occurrence of SLWCs, classified as non-
87 precipitating, drizzling, or raining clouds based on CloudSat column maximum radar reflectivity. The second
88 diagnostic is the CFODD, which is the probability density function (PDF) of radar reflectivity as a function of in-
89 cloud optical depth (ICOD), where ICOD is the optical depth integrated from the cloud top downward to each vertical
90 layer and represents an in-cloud vertical coordinate (Nakajima et al., 2010; Suzuki et al., 2010). The CFODD shows
91 how vertical cloud microphysical structures transition from non-precipitating to precipitating as a function of cloud-
92 top effective radius (R_e), and the slope of reflectivity change with ICOD provides an estimate of droplet collection
93 efficiency factor (Suzuki et al., 2010). Previous studies have used CFODDs to demonstrate that pollution decreases
94 droplet collection efficiency, suppressing rainfall near the cloud base (Mangla et al., 2020; Michibata et al., 2014;
95 Suzuki et al., 2013), and to evaluate model cloud liquid to rain conversion processes against satellite observations
96 (Suzuki et al., 2015; Jing et al. 2019; Michibata and Suzuki, 2020). Takahashi et al. (2021) proposed an updated
97 CFODD analysis in which R_e thresholds are defined by quartile distributions of SLWC samples rather than the
98 traditional CFODD R_e thresholds to focus evaluation on warm rain process representation rather than the bias in R_e
99 distribution. Modifications to the WRDs in the present study include additional diagnostics that provide SLWC
100 sampling statistics to illuminate how sample size affects CFODD results, the implementation of a CloudSat ground-
101 clutter mask in the simulated WRDs and updates to SLWC selection criteria for better consistency between
102 observations and satellite simulators. The updated CFODD analysis is demonstrated here as a constraint on the
103 component of ER_{Facisw} that is affected by droplet collection efficiency due to autoconversion.

104 **2 Warm Rain Diagnostics Overview**

105 The WRDs and their implementation in COSPv2.0 were described in Michibata et al. (2019). The WRDs are designed
106 to run online with the host model, accumulating time step statistics on warm rain cloud processes for subcolumns to
107 mitigate the risk of data-processing bottlenecks associated with outputting large data volumes. COSPv2.0 generates
108 ensembles of stochastic subcolumns from model gridbox-mean variables to emulate model subgrid variability and to
109 resolve discrepancies in spatial resolution between observations and the model grid (Swales et al., 2018).

110 To generate observational reference data for model evaluation, Michibata et al. (2019) used the MODIS and CloudSat
111 products 2B-TAU R04 (Polonsky, 2008) and 2B-GEOPROF R04 (Mace et al., 2007; Marchand et al., 2008),

112 respectively, for SLWC detection between June 2006 and April 2011. The SLWC detection are described in
 113 Supplement Table S1 and include CloudSat reflectivity ≥ -30 dBZ, MODIS liquid COT > 0.3 , and cloud top
 114 temperature ≥ 273 K. Model-simulated SLWCs are detected using COSPv2.0 simulated CloudSat reflectivity and
 115 multiple MODIS cloud properties, including ice water path (IWP), liquid water path (LWP), cloud-top effective radius
 116 (R_e), and cloud optical thickness (COT) (Table S1). For the SLWC fractional occurrence (frequency) diagnostic,
 117 SLWCs are binned by precipitation intensity according to the maximum column CloudSat reflectivity (Z_{max}), where
 118 non-precipitating, drizzling and raining SLWCs correspond to $Z_{max} < -15$ dBZ_e, -15 dBZ_e $\leq Z_{max} < 0$ dBZ_e,
 119 and $Z_{max} \geq 0$ dBZ_e, respectively. The SLWC fractional occurrence diagnostic features frequency of each
 120 precipitation type relative to the total SLWC population.

121 To support evaluation of liquid cloud collection efficiencies and cloud to rain transition processes, CFODDs are
 122 constructed from the PDFs of CloudSat reflectivity profiles binned by ICOD. ICOD (τ_d) is parameterized as a function
 123 of MODIS COT (τ_c) by invoking the adiabatic condensation growth model to vertically slice the column COT into
 124 each layer (Suzuki et al., 2010). The relationship between τ_d and τ_c is as follows:

$$125 \quad \tau_d(h) = \tau_c \left\{ 1 - \left(\frac{h}{H} \right)^{5/3} \right\} \quad (1)$$

126 where h is height and H is the geometric height of the cloud. The detailed derivation of the ICOD coordinate is
 127 provided in Suzuki et al. (2010). The slope of the resulting 2D-PDF diagnostic is modulated by droplet collection
 128 efficiency, with steeper slope implying higher efficiency. The CFODD shows where, with ICOD on the y-axis as a
 129 vertical coordinate, the droplet collection efficiency increases, and where the transition from non-precipitating to
 130 drizzling and raining occurs, using the radar reflectivity as a proxy for the precipitation rate as described above (e.g.,
 131 Muhlbaeuer et al., 2014). CFODDs are also typically binned by R_e to reveal how droplet collection efficiency changes
 132 with droplet size (Suzuki et al., 2010; Takahashi et al., 2021; Jing et al., 2017).

133 In this study, CFODD slopes are estimated using RANdom SAMple Consensus (RANSAC) robust linear regression
 134 (Fischler et al., 1987). RANSAC was chosen for performing linear regression due to the right-skewed distribution of
 135 CFODD datasets. The regression was applied to the MODIS-CloudSat profiles and E3SMv2 output at $4 \leq \text{ICOD} \leq 20$
 136 and $Z < 20$ dBZ. For E3SMv2 output, the regression was applied to approximated source CloudSat reflectivity and
 137 ICOD data that was estimated from time-mean CFODD frequencies. The reflectivity and ICOD thresholds were were

138 chosen to reduce the effect of the Mie scattering regime where the radar reflectivity can be saturated and to restrict
139 analysis to profiles where the uncertainty of MODIS COT retrievals is lower as error can be higher in optically thin
140 liquid clouds (e.g., $COT < 4$) (Platnick et al., 2017). The uncertainty in the RANSAC slope calculation is estimated
141 by “bootstrapping”, repeatedly performing RANSAC regressions on 1000 random subsamples of 80% the CFODD
142 dataset to generate a distribution of slope estimates. The 1-sigma error and 95% confidence intervals were calculated
143 from this distribution. The residual threshold applied for RANSAC outlier detection was 0.1 and $0.5 \times$ median absolute
144 error (MAE) for MODIS-CloudSat and E3SMv2, respectively. Data points with MAE exceeding the residual threshold
145 are excluded from the linear regression in RANSAC.

146 **2.1 E3SMv2**

147 Several updates to the WRDs are described in Sect. 2.2, the impacts of which are demonstrated through an application
148 of the updated WRDs to the U.S. Department of Energy’s Energy Exascale Earth System Model v2 (E3SMv2). The
149 atmosphere component of the model, E3SM Atmosphere Model v2 (EAMv2), is described in detail in Golaz et al.
150 (2022). Like its predecessor EAMv1, EAMv2 predicts stratiform and shallow cumulus cloud macrophysics through
151 the Cloud Layers Unified by Binormals (CLUBB) parameterization, which unifies the treatment of planetary boundary
152 layer turbulence, shallow convection, and cloud macrophysics through a higher-order turbulence closure scheme
153 (Bogenschutz et al., 2013; J. C. Golaz et al., 2002; Larson, 2017; Larson & Golaz, 2005). CLUBB diagnoses cloud
154 fraction and cloud liquid water from a joint double-Gaussian PDF. Ice and liquid cloud fractions in CLUBB are
155 analytically diagnosed by integrating saturated proportions of the joint PDF (Guo et al. 2015).

156 Cloud microphysics is represented with the “Morrison and Gettelman version 2” (MG2) scheme (Gettelman and
157 Morrison, 2015). MG2 prognoses the mass mixing ratios and number concentrations of cloud liquid, ice and
158 precipitation hydrometeors. The coupled MG2 cloud microphysics and CLUBB higher-order turbulence
159 parametrization explicitly provides values for hydrometer mass and number mixing ratios as well as cloud fraction.
160 Deep convection is represented by the Zhang and McFarlane (1995) (ZM) scheme. As convective cloud fraction is
161 not parameterized in the mass-flux based ZM scheme, it is diagnosed from the cloud mass flux for cloud radiation
162 calculation (Hack et al., 1993). The total cloud fraction in EAMv2 combines CLUBB, deep convective cloud fractions
163 and ice cloud fraction following (Park et al., 2014). The four-mode version of the Modal Aerosol Module (MAM4) is
164 used to predict aerosol properties and processes (Liu et al., 2012, 2016; H. Wang et al., 2020).

165 EAMv2 runs on 72 vertical atmospheric levels with a top at 0.1h Pa (Rasch et al., 2019; Xie et al., 2018). However,
166 distinct from its predecessor EAMv1, EAMv2 has two separate parameterized physics and dynamics grids (Hannah
167 et al., 2021), with average horizontal grid spacings of ~165 km and ~110 km, respectively.

168 A six-year E3SMv2 simulation with transient, present-day forcing was run between 2006 and 2011 with online
169 COSPv2.0 for comparison with A-Train observations of SLWCs, allowing one additional year (2005) for model spin-
170 up. To facilitate comparison with observations, large-scale winds were constrained via the “nudging” technique (Lin
171 et al., 2016; Ma et al., 2014; Zhang et al., 2014), in which horizontal and vertical winds are relaxed toward the Modern
172 Era-Retrospective Analysis for Research and Applications, Version 2 (MERRA2) reanalysis data (Gelaro et al., 2017)
173 with a 6-hour time-scale. MERRA2 data are read in every 3 hours and linearly interpolated to model times. COSPv2.0
174 is called at every time step (0.5 h) and run with 10 subcolumns. We observed little change in CFODD results for
175 increased numbers of subcolumns of 20 to 50.

176 **2.2 COSPv2.0**

177 Cloud-observing instrument simulators support evaluation of model cloud representation by translating gridbox-mean
178 model variables (e.g., cloud fraction, hydrometeor mass mixing ratio, precipitation) into quantities that are measured
179 by a cloud sensor (e.g., reflectivity). COSPv2.0 includes multiple cloud-observing satellite simulators and has been
180 used extensively to diagnose issues in model cloud representation (Cesana & Chepfer, 2012; Kay et al., 2016; Song
181 et al., 2018a; Y. Zhang et al., 2010). Recently, M. Zhang et al. (2022) used the COSPv2.0 CALIPSO simulator to
182 demonstrate that changes to the Wegener-Bergeron-Findeisen process in EAMv2 decreased an ice cloud fraction low
183 bias in the Arctic compared to EAMv1 but did not correct excesses of supercooled liquid.

184 There are known limitations to COSPv2.0 that affect its application to E3SM for cloud representation evaluation. The
185 subgrid distribution of cloud variables generated by COSPv2.0 does not match E3SM subgrid variability.
186 Hydrometeor species are distributed homogeneously across the subcolumns generated by COSPv2.0 via the
187 subcolumn generator SCOPS (Subcolumn Cloud Overlap Profile Sampler) (Klein and Jakob, 1999), such that the
188 ensemble of subcolumns reproduces the gridbox cloud fraction but not the subgrid distribution of liquid and ice within
189 the simulated clouds (Dewald, 2021). Song et al., (2018b) demonstrated that the default “homogeneous hydrometeor
190 scheme” from SCOPS results in overestimation of radar reflectivity in warm liquid clouds, thus overestimating
191 precipitating clouds since maximum column reflectivity is often used to distinguish precipitating clouds (as in the

192 WRDs). Errors in simulated satellite retrievals have also been attributed to SCOPS overlap assumptions (Hillman et
193 al., 2018). Such a bias from SCOPS can result in unfair observational evaluation of a host model such as E3SMv2.
194 Inconsistencies in microphysical assumptions between the host model and COSP pose another challenge. While many
195 microphysical assumptions in COSPv2.0 can be configured for agreement with E3SMv2 microphysics (MG2), some
196 inconsistencies remain, including gamma distribution shape parameters for hydrometeor size distributions and
197 hydrometeor vertical overlap assumptions (J. Wang et al., 2021). Next-generation E3SM development includes efforts
198 to improve agreement in the subgrid variability and microphysical assumptions involved in forward simulating
199 satellite retrievals. Other issues include the simplified treatment of satellite cloud detection in simulators. For example,
200 the CloudSat Cloud Profiling Radar (CPR) cloud mask value threshold ≥ 30 is applied for cloud detection in the
201 WRDs' A-Train analysis to indicate "good" or "strong" echo with high confidence detection (see next section and
202 Supplement Table 1). The CPR cloud mask confidence levels consider signal-to-noise ratios, horizontal averaging,
203 and spatial continuity (Marchand et al., 2008), but as this cloud mask is not available in COSPv2.0, CloudSat cloud
204 detection is simulated by applying a reflectivity threshold $-30 \leq Z_e \leq 20$ dBZ.

205 The WRDs rely on COSPv2.0 simulated MODIS and CloudSat retrievals. The WRDs in COSPv2.0 work as
206 follows: First, COSPv2.0 takes in model atmospheric state and cloud variables including temperature, pressure,
207 water vapor and hydrometeor mass mixing ratios, hydrometeor R_e , large-scale stratiform cloud fraction, convective
208 cloud fraction and precipitation rate. The COSPv2.0 subcolumn generator SCOPS then produces subgrid
209 distributions of clouds and precipitation for better comparison with smaller scale satellite pixel measurements.
210 SCOPS subcolumns are homogenous, discrete samples generated such that a sufficiently large ensemble reproduces
211 the model column profile of bulk cloud properties (Webb et al., 2001; Swales et al., 2018). SCOPS assigns each
212 subcolumn a type (large-scale stratiform, convective or clear-sky) according to the host model's convective and
213 large-scale stratiform cloud fraction. Cloud properties such as hydrometeor mass mixing ratios and R_e are distributed
214 homogeneously across the subcolumns by cloud type (i.e., all stratiform cloud subcolumns are assigned the same
215 stratiform ice and liquid mixing ratios as SCOPS only takes total convective and stratiform cloud fraction as input,
216 and does not consider stratiform liquid and ice cloud fraction in its default configuration. "Maximum-random"
217 cloud overlap is applied to subcolumns, consistent with the model parameterizations. The MODIS and CloudSat
218 simulators apply simplified versions of their respective retrieval algorithms to each subcolumn, emulating MODIS
219 retrievals of cloud properties, radar reflectivity and lidar backscatter, respectively. Gridbox-mean values are

220 estimated from accumulated subcolumn statistics. The WRDs take as inputs gridbox-mean simulated MODIS
221 retrievals of LWP, IWP, COT and R_e , as well as subcolumn CloudSat reflectivity profiles. The simulated MODIS
222 COT represents in-cloud mean, as do the other MODIS variables used in the WRDs (e.g., LWP, R_e). For example,
223 the MODIS liquid COT is computed by averaging the MODIS liquid COT in cloudy subcolumns across the grid-
224 box. In E3SMv2-COSP, the same in-cloud stratiform COT value from the E3SMv2 radiative transfer module is
225 distributed across all the subcolumns designated as stratiform cloud by SCOPS, as described above. These values
226 and cloud/clear-sky designations for each subcolumn are used as input to the MODIS simulator to calculate the in-
227 cloud MODIS liquid COT. Subcolumn-level SLWC reflectivity profiles are used as input to the WRDs, also with
228 cloud properties homogeneously distributed across the subcolumns of a given classification. Thus, in E3SM-COSP,
229 the SLWC samples within a gridbox that have the same subcolumn classification (i.e., stratiform liquid or stratiform
230 rain) will have the same simulated MODIS COT and CloudSat reflectivity profile.

231 Deviations from the original WRDs implemented in COSPv2.0 (Michibata et al., 2019b) include the application of
232 the simulated CloudSat ground-clutter filter (available in COSPv2.0, but not applied to the WRDs previously) for
233 better comparison with CloudSat retrievals, and the elimination of the “fracout” input used in the SLWC detection
234 scheme from SCOPS. “Fracout” is the subcolumn-level cloud classification by vertical level from SCOPS, where each
235 level of each subcolumn is designated as large-scale stratiform, convective, or clear-sky. This input was removed from
236 the WRDs’ SLWC detection algorithm because of the lack of comparable cloud-type designation in the observations
237 and CloudSat simulator and because “fracout” vertical cloud profiles were observed to deviate significantly from
238 CloudSat reflectivity profiles (i.e., fracout indicates clear-sky where CloudSat reflectivity indicates cloud, or vice
239 versa).

240 **2.3 Satellite data**

241 The MOD06-1KM-AUX R05 product (Platnick et al., 2017), which provides MODIS collection 6 retrievals at 1 km
242 resolution along the CloudSat footprint, supplied the 6 MODIS cloud retrievals required for the SLWC detection
243 described in Suzuki et al. (2010): LWP, IWP, R_e , COT, cloud top pressure and cloud layer number. Standard MODIS
244 products from the 2.1 μm channel were used for R_e , consistent with the simulated MODIS R_e used in the WRDs.
245 Atmospheric temperature profiles were obtained from ECMWF-AUX R05 (Partain and Cronk, 2017), which includes
246 temperature profiles from the European Centre for Medium-Range Weather Forecast (ECMWF) model (Dee et al.,

247 2011) interpolated to the CloudSat footprint. 2B-GEOPROF R05 provided the CloudSat reflectivity profiles, the Cloud
248 Profiling Radar (CPR) cloud mask and echo top characterization at 1.8 km resolution (Marchand et al., 2008). The
249 detection of SLWCs and CFODD analysis in the present study follows Suzuki et al. (2010) (see Supplement Table 1
250 for details) with one exception: a COT threshold was decreased from 15 to 0.3; this had a substantial impact on cloud
251 occurrence (Figure 1; described next) and is consistent with the COT threshold implemented in the COSPv2.0 WRDs.
252 The decreased COT threshold also increases the weight of optically thin SLWCs, as the linear regression is applied to
253 the CFODD source data directly (i.e., the ICOD and reflectivity profiles).

254 **2.4 Autoconversion sensitivity experiments and ERFaci**

255 The autoconversion parameterization in E3SMv2 is a modified Khairoutdinov & Kogan (2000) scheme (hereafter,
256 KK2000), in which coefficients were updated in response to large uncertainties in different cloud regimes and to
257 improve fidelity in climate simulations. The KK2000 autoconversion scheme is $\frac{\delta q_r}{\delta t_{auto}} = A Q_c^\alpha N_d^\beta$, where q_r is
258 the rainwater mixing ratio, Q_c is the cloud water mixing ratio, N_d is the cloud droplet number concentration, and A , α
259 and β are the modified coefficients.

260 To develop a constraint on the ERFaci due to autoconversion, we performed multiple pairs of simulations featuring
261 preindustrial (PI) and present-day (PD) aerosol emissions. In each pair of simulations, one of the three coefficients
262 (A , α or β) was modified to its KK2000 value, a value reported by Wood (2005), a value from Kogan (2013) or a value
263 within a range bounded by the three studies. The Kogan (2013) coefficient values were derived from a large-eddy
264 simulation (LES) with bin resolved microphysics for cumulus clouds, whereas the focus of Wood (2005) and KK2000
265 was stratocumulus clouds from observational and LES perspectives, respectively. One additional experiment on the
266 KK2000 parameterization for the accretion rate was performed, the formulation of which is $\frac{\delta q_r}{\delta t_{accre}} =$
267 $F_1 F_2 67 (Q_c Q_r)^{1.15} \rho^{-1.3}$, where Q_r is the rain water mixing ratio, F_1 represents subgrid Q_c variability, ρ is air density,
268 and F_2 is an accretion rate enhancement factor. F_2 was increased by a factor of ~ 3 in the accretion sensitivity
269 experiment. F_2 is considered a tunable parameter in E3SM (Ma et al., 2022). The experiment details are provided in
270 Table 1.

271 Table 1. KK2000 coefficient and accretion enhancement factor values applied in 12 sensitivity experiments. Dash (“-”
 272 “) indicates the coefficient value was unchanged from the default E3SMv2 parameterization (equal to the “CNTL”
 273 simulation value).

Name	A	α	β	accre
CNTL	3.05E4	3.19	-1.4	1.75
alpha01	-	4.22	-	-
beta01	-	-	-1.0	-
acoef100x	3.05E6	-	-	-
alpha02	-	2.47	-	-
acoef0.05x	1.35E3	-	-	-
alpha03	-	3.00	-	-
beta03	-	-	-1.79	-
beta04	-	-	-3.01	-
acoef10x	3.05E5	-	-	-
acoef5x	1.53E5	-	-	-
acoef50x	1.53E6	-	-	-
accre01	-	-	-	5

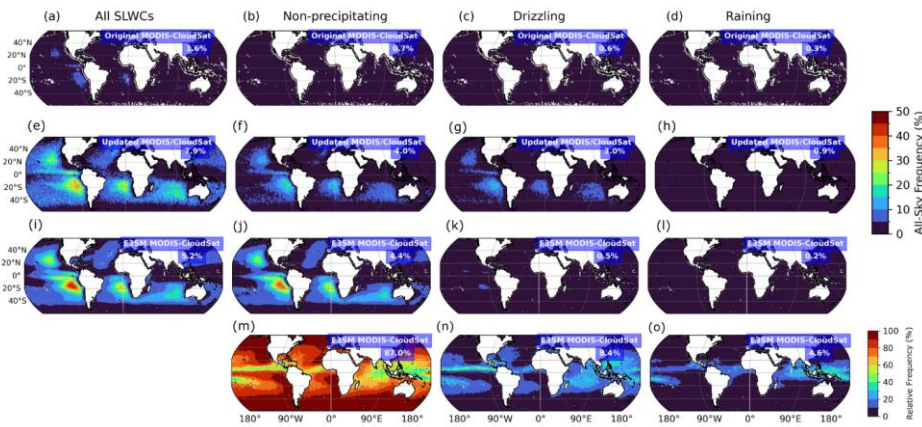
274

275 ERF_{aci} for each pair of simulations was calculated following the Ghan (2013) method, where $ERF_{aci} = \Delta(F_{clean} -$
 276 $F_{clear, clean}) \cdot F_{clean}$ is the radiative flux at the top-of-atmosphere (TOA) neglecting the absorption and scattering of
 277 aerosols, and $F_{clear, clean}$ is the radiative flux at the TOA neglecting both clouds and the absorption and scattering of
 278 aerosols. The Δ indicates the PD – PI difference. While the PD-PI approach is a common strategy for estimating
 279 ERF_{aci}, Christensen et al. (2023) demonstrated that it may yield a different estimate than the PD approach, where
 280 components of ERF_{aci} (LWP adjustment, N_d adjustment, cloud fraction adjustment) are estimated by regressions of
 281 cloud properties multiplied by the anthropogenic aerosol fraction. We calculate ERF_{aci} for SLWCs only, binned by
 282 the MODIS R_e range corresponding to the CFODD analysis.

283 A constraint on $ERFac_{iSW}$ was calculated from the linear regression between E3SMv2 CFODD slopes and $ERFac_{iSW}$,
 284 using the MODIS-CloudSat CFODD slope as a reference. A 95% confidence interval for the linear fit was estimated
 285 by bootstrapping the linear regression within the uncertainty of the CFODD slopes. CFODD slope values were
 286 randomly sampled 1000 times within their 1-sigma error and repeatedly regressed with $ERFac_{iSW}$. The original data
 287 (i.e., RANSAC CFODD slope values and corresponding $ERFac_{iSW}$ values) were additionally resampled with
 288 replacement to generate a distribution of coefficients for the ordinary least squares (OLS) regression. The 95%
 289 confidence interval for the linear fit was then calculated from the combined linear regression coefficient distributions
 290 to reflect uncertainty from both the OLS fit and the CFODD slopes.

291 3 Updates to MODIS and CloudSat SLWC analysis and reference data

292 The first diagnostic in the original WRDs featured relative frequencies of SLWCs by precipitation intensity in both
 293 the A-Train reference data and the COSPv2.0 output (e.g., Fig. 1 m-o). We have updated this diagnostic with all-sky
 294 frequencies and by decreasing the lower MODIS COT threshold from 15 to 0.3, for consistency with the WRDs
 295 implemented in COSPv2.0 (Fig. 1 a-l). SLWCs featured in Fig. 1 and all following figures and analyses are ocean-
 296 only due to higher uncertainties in MODIS retrievals over land (Platnick et al., 2017).



297
 298 **Figure 1.** All-sky frequencies of total SLWCs June 2006 – Apr 2011, non-precipitating ($Z_{max} < -15 \text{ dBZ}_e$), drizzling
 299 ($-15 \text{ dBZ}_e \leq Z_{max} < 0 \text{ dBZ}_e$) and raining ($Z_{max} \geq 0 \text{ dBZ}_e$) ocean-only SLWCs according to original reference analysis of
 300 MODIS and CloudSat observations (Michibata et al., 2019a, 2019b) (a-d), updated reference MODIS and CloudSat analysis (e-h)

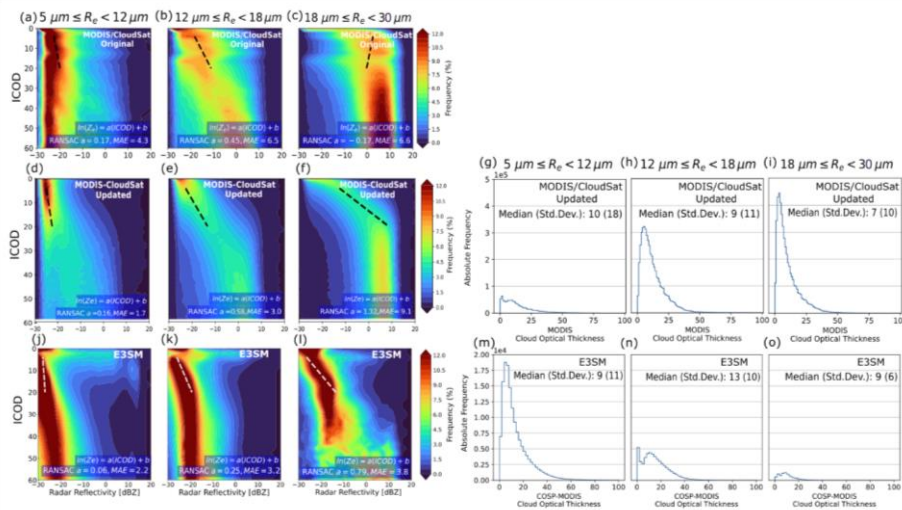
301 and E3SMv2-COSPV2.0 (i-l). Figures m-o show frequencies of non-precipitating, drizzling and raining SLWCs relative to the total
302 SLWCs simulated by E3SMv2. Values in blue boxes indicate global ocean-only grid-weighted mean frequency. SLWCs were
303 undersampled in original reference A-Train analysis by a factor of ~5. Compared to the original reference A-Train data, the updated
304 analysis demonstrates that E3SM underrepresents rather than overrepresents total SLWC frequency and that precipitating SLWCs
305 are underrepresented by a factor of 6 compared to observations.

306 Figure 1 also shows that decreasing the lower MODIS COT threshold from 15 to 0.3 in the updated A-Train analysis
307 (Sect. 2.3) increased total SLWC sampling by 5-fold (global ocean mean, see Sect. 2.3) compared to the original
308 CFODD analysis in Michibata et al. (2019a) and Michibata et al. (2019b). The increase in SLWC sampling in the
309 reference data affects multiple outcomes of the model evaluation in this case: E3SMv2 underrepresents, rather than
310 overrepresents, total SLWCs, and the SLWCs that are missing from E3SMv2 are entirely the precipitating SLWC
311 populations. The underrepresentation of precipitating SLWCs in E3SMv2-COSP indicates that any bias from SCOPS
312 towards increased precipitation in warm liquid clouds is relatively minor (Sect. 2.2; Song et al. (2018)). Not all the
313 differences between the original and updated reference data can be explained by the change in COT threshold,
314 however, as we were unable to reproduce the original CFODD data with the updated satellite products used in this
315 study. Fig. S1 and S2 show that increasing the lower COT threshold from 0.3 to 15 yields SLWC frequencies that are
316 much closer to the original reference data (+25%) than the updated reference data, but significant differences remain
317 in the CFODDs.

318 The effects of the increased SLWC sampling in the A-Train reference data also significantly affected the CFODDs
319 and thus the comparison between A-Train and E3SMv2 droplet collection efficiencies. Figure 2 shows CloudSat
320 reflectivity frequency binned by ICOD for the original A-Train reference data (Fig. 2 a-c), the updated A-Train
321 reference data (d-f) and E3SMv2 (j-l), and RANSAC robust linear regression slopes at $4 \leq \text{ICOD} \leq 20$. In comparisons
322 with various other linear regression techniques, we found that RANSAC best supported the comparison of CFODD
323 slopes between E3SMv2 and observations because of the right-skewed distribution of CloudSat reflectivities at $0 \leq$
324 $\text{ICOD} \leq 20$ in E3SMv2 CFODDs (Figs. 2 j-l). RANSAC minimizes the median absolute error (MAE) and is less
325 sensitive to strong outliers in the dimension of the predicted variable (Z_e in this case) compared to other linear
326 regression techniques.

327 The updated A-Train CFODD distributions are significantly different than the original CFODD distributions (2D-
328 Kolmogorov-Smirnov test, $p \ll 0.05$). Compared to updated A-Train CFODDs, the E3SMv2 CFODDs show

329 decreased droplet collection efficiencies and an increased range of reflectivities near the cloud top in all size bins,
 330 indicating that regardless of R_e , SLWCs are drizzling and raining near the cloud top with significantly higher frequency
 331 than SLWCs in observations but have decreased collection efficiency below cloud top compared to MODIS-CloudSat.
 332



333
 334 **Figure 2.** Contoured frequency by optical depth diagrams (CFODDs) for SLWCs June 2006 – April 2011 binned by MODIS cloud
 335 top effective radius (R_e) from original reference MODIS-CloudSat observations analysis (a-c), updated reference MODIS-CloudSat
 336 observations analysis (d-f), and E3SMv2 (j-l). Random Sample Consensus (RANSAC) linear regressions were applied to the
 337 CFODD at $4 \leq \text{ICOD} \leq 20$ to estimate droplet collection efficiencies. RANSAC slopes and Median Absolute Error (MAE) values
 338 are shown in blue boxes. Droplet collection efficiencies increase with MODIS R_e as expected, except for the largest R_e size bin in
 339 the original reference data (Fig. s2c). Figs. g-i and m-o show absolute frequencies of SLWCs by MODIS COT, demonstrating that
 340 E3SMv2 overrepresents SLWCs with small R_e relative to medium and large R_e , compared to observations.

341 The high reflectivities near the cloud top are pronounced in the subset of E3SMv2 SLWCs with $4 < \text{MODIS COT} <$
 342 20 (Fig. S3), indicating that the high reflectivity at low ICOD in Figs. 2 (j-l) is not just a product of a subset of
 343 precipitating, optically thin SLWCs, but that layers near the cloud top in deeper SLWCs are also precipitating, also
 344 contribute. The reflectivity profiles used to generate the CFODD come from the CloudSat simulator, which was not

345 modified for this study. Examples of simulated CloudSat reflectivity profiles in SLWCs with $Z_e > 0$ dBZ near cloud
346 top are shown in Fig. S4. The source of this issue and its implications for E3SMv2 representation of liquid cloud
347 properties warrant further investigation that is beyond the scope of the present study.

348 Figure 2 shows absolute frequencies of SLWCs binned by MODIS COT in each CFODD R_e bin for the updated A-
349 Train analysis (Fig. 2 g-i) and E3SMv2 only (Fig. 2 m-o). Note, this information was unavailable in the original
350 reference data (Michibata et al., 2019a). Compared to COT distributions in the updated A-Train analysis, E3SMv2
351 shows decreasing SLWC frequency with R_e and an underrepresentation of SLWCs with large R_e , which aligns with
352 the underrepresentation of precipitating SLWCs in Fig. 1. Fig. 2o also shows that few SLWCs with large R_e have a
353 COT > 20 , indicating that the CFODD reflectivity profile in Fig. 2l at ICOD > 20 is comprised of few samples. The
354 SLWC COT PDFs have been implemented in the WRDs to support the interpretation of CFODD statistics.

355 **4 Results and Discussion**

356 **4.1 CFODD analysis to constrain ERFaci due to warm rain processes**

357 To demonstrate the potential of the CFODD analysis described above for constraining ERFaci_{SW} due to warm rain
358 processes, we performed 12 experiments featuring variations of E3SMv2's autoconversion and accretion
359 parameterizations, computing ERFaci_{SW} for the SLWC samples represented in each CFODD and the corresponding
360 R_e bin (hereafter, "ERFaci_{SW_SLWCs}") following Ghan (2013; see Sect. 2.4). In each experiment, a single coefficient of
361 either the KK2000 autoconversion or accretion parameterization was perturbed, each of which is treated as a tunable
362 parameter in E3SMv2. The uncertain KK2000 coefficients, coupled with parameterization simplifications (e.g., bulk
363 moments and assumed droplet size distributions), result in uncertainties and biases in the model representation of
364 raindrop formation and growth. The experiments are described in Table 1, and the CFODDs for each experiment are
365 shown in Fig. S5.

366 Figure 3 shows a strong negative correlation between E3SMv2 ERFaci_{SW_SLWCs} with "small" or "medium" R_e (i.e., 5
367 $\leq R_e < 18 \mu\text{m}$) and the corresponding combined $5 \leq R_e < 18 \mu\text{m}$ CFODD slope (Pearson's $R = -0.91$). SLWCs with
368 large R_e ($18 \leq R_e < 30 \mu\text{m}$) were excluded from the analysis in Fig. 3 because this population represents a negligible
369 fraction of total SLWCs in E3SMv2 (see Fig. S6), resulting in poor sampling statistics and larger regression
370 uncertainties. As CFODD slopes represent an estimate of droplet collection efficiency, Fig. 3 demonstrates that

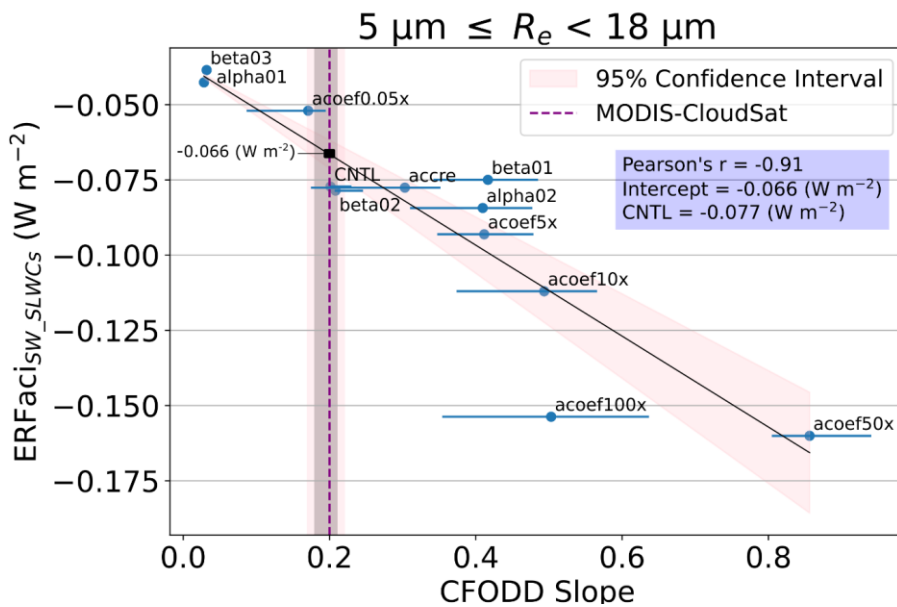
371 ERFaci_{sw} strengthens (increases in magnitude) with increasing droplet collection efficiency in E3SMv2 SLWCs with
372 R_e between 5 and 18 μm . One possible physical explanation for the relationship between autoconversion, droplet
373 collection efficiency, and ERFaci_{sw} is that increased autoconversion rates increase the susceptibility of clouds to
374 precipitation suppression by aerosols. For a given optical depth, SLWCs with lower LWP and/or higher N_d will
375 precipitate more when the autoconversion rate is increased. A larger population of precipitating SLWCs results in
376 increased susceptibility to precipitation suppression by aerosols overall. When aerosols suppress precipitation (e.g.,
377 Suzuki et al., 2013), LWP and/or cloud fraction may be enhanced, resulting in brighter clouds and stronger ERFaci_{sw}.
378 The relationship between aerosols, LWP and cloud fraction (Albrecht, 1989), however, is highly uncertain, varies
379 regionally (Sato et al., 2018), and is influenced by processes that are buffered over multiple spatiotemporal scales
380 (Stevens and Feingold, 2009). Additionally, E3SMv2's CFODD slope ("CNTL" simulation) agrees with MODIS-
381 CloudSat within uncertainty, indicating that droplet collection efficiency is well-represented according to CFODD
382 analysis.

383

384

385

386



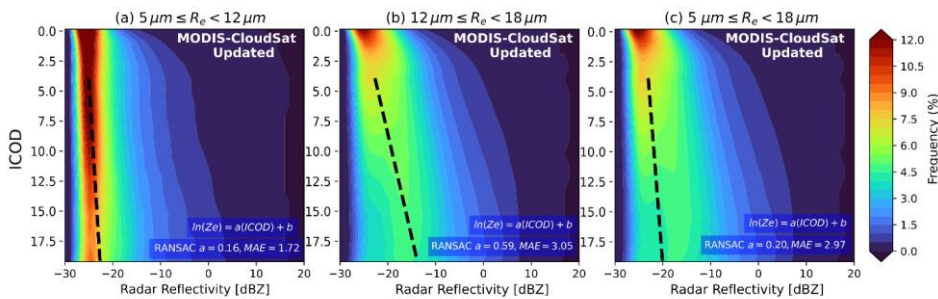
387
 388 **Figure 3.** Linear regression between E3SMv2 $ERFacisw_{SLWCs}$ and CFODD slopes, generated from SLWCs with MODIS R_e
 389 between 5 and 18 μm , in 12 PD autoconversion and accretion sensitivity experiments. $ERFacisw_{SLWCs}$ values reflect the SLWCs
 390 represented in the corresponding CFODD (i.e., with R_e corresponding to the CFODD R_e bin). Results show a strong negative
 391 correlation between E3SMv2 $ERFacisw_{SLWCs}$ and CFODD slopes. We constrain the $ERFacisw$ by predicting the $ERFacisw_{SLWCs}$
 392 value at the reference MODIS-CloudSat $5 \leq R_e < 18 \mu m$ CFODD slope (purple dashed line) from the linear regression (intercept
 393 shown in blue box). ~~The constrained $ERFacisw$ value is decreased by $14 \pm 6\%$ in magnitude compared to the CNTL simulation.~~
 394 Error bars represent 1-sigma error estimated from RANSAC-fit bootstrapping (Sect. 2). Grey and pink shaded regions indicate the
 395 68 and 95% confidence intervals for the MODIS-CloudSat CFODD slope, respectively. Labels indicate the sensitivity experiment
 396 names (Table 1).

397 In Figure 3, we constrain $ERFacisw$ due to autoconversion uncertainties using the linear regression between the
 398 simulated CFODD slopes and $ERFacisw_{SLWCs}$. $ERFacisw$ and $ERFacisw_{SLWCs}$ values were calculated following Ghan
 399 et al. (2013), which considers the difference in TOA radiative flux between the PD and PI experiments, neglecting
 400 direct forcing of aerosols (see Sect. 2.4 for details). ~~We estimated TheThe~~ constrained value of $ERFacisw_{SLWCs}$ is
 401 ~~estimated~~ at the intercept of the linear relationship with the observed MODIS-CloudSat CFODD slope (Fig. 4). ~~We~~

Formatted: Font: (Default) Times New Roman, 10 pt

402 find that the $ERFac_{SW_SLWCs}$ predicted by the linear regression at the MODIS-CloudSat slope value ($-0.066 \text{ W m}^{-2} \pm$
 403 0.06 W m^{-2}) approaches agreement with the $ERFac_{SW_SLWCs}$ value predicted by the E3SMv2 CNTL simulation (-0.077
 404 W m^{-2}), particularly considering the additional uncertainties imposed by the limited number of sensitivity experiments
 405 that are not represented in the regression's 95% confidence interval. The agreement between the constrained and
 406 predicted value of $ERFac_{SW_SLWCs}$ indicates that the $ERFac_{SW}$ due to autoconversion is well-represented in E3SMv2
 407 according to CFODD analysis. The $ERFac_{SW_SLWCs}$ predicted by the linear regression at the MODIS-CloudSat slope
 408 value is -0.066 W m^{-2} , a $14 \pm 6\%$ decrease in magnitude compared to the $ERFac_{SW_SLWCs}$ value predicted by the
 409 E3SMv2 CNTL simulation (-0.077 W m^{-2}). E3SMv2's total $ERFac$ (-1.50 W m^{-2}), inclusive of all cloud types and the
 410 longwave forcing component, falls within the IPCC AR6 'very likely' range for $ERFac$ ($-1.0 \pm 0.7 \text{ W m}^{-2}$). The
 411 shortwave component of $ERFac$ is significantly larger than longwave in CMIP6 models (e.g., multimodel means of
 412 -0.91 and $+0.10 \text{ W m}^{-2}$, respectively, as reported in Smith et al. 2020). Thus, our results indicate that eliminated the
 413 bias in $ERFac_{SW}$ due to autoconversion uncertainties would decrease the magnitude of $ERFac_{SW}$ and bring the
 414 predicted total $ERFac$ closer to the median IPCC $ERFac$ value (Forster et al., 2021).

Formatted: Font: (Default) Times New Roman, 10 pt



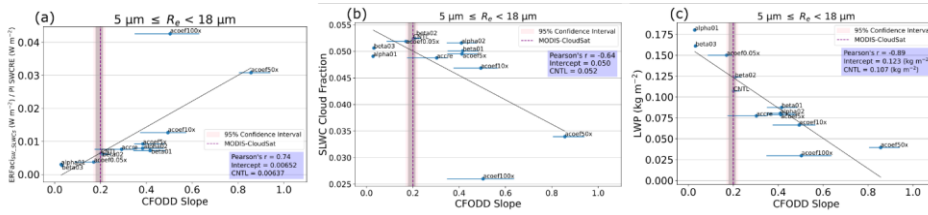
415
 416 **Figure 4.** CFODDs for subset of SLWCs with max CloudSat reflectivity < 20 dBZ and COT < 20, June 2006 – April 2011, binned
 417 by MODIS R_e from updated reference MODIS-CloudSat observations analysis (a-b), and with combined “small” and “medium”
 418 R_e SLWCs in (c). RANSAC linear regressions were applied to the CFODD at $4 \leq ICOD \leq 20$ to estimate droplet collection
 419 efficiencies. RANSAC slopes and Median Absolute Error (MAE) values are shown in blue boxes.

420 As $ERFac_{SW}$ is the result of many cloud processes, the updated CFODD analysis should be interpreted as a constraint
 421 on the component of $ERFac_{SW}$ that is modulated by droplet collection efficiency due to autoconversion. In other
 422 words, the updated CFODD analysis shows the change in $ERFac_{SW}$ one would expect if the bias in $ERFac_{SW}$ due to

423 a specific process representation affecting droplet collection efficiency were eliminated. Base cloud processes that are
424 independent of aerosol also contribute significantly to ERF_{aci} estimates (Mülmenstädt et al., 2020). Autoconversion
425 perturbations affect base cloud state (e.g., LWP, cloud fraction) and could, for example, cause stronger ERF_{aci} by
426 increasing cloud amount rather than increasing the impact of ACI on SW radiative forcing. Jing et al. (2019) evaluated
427 different autoconversion parameterization schemes in an ESM using the CFODD analysis described in Michibata et
428 al. (2019b) and found that the autoconversion scheme that yielded the best warm rain representation predicted a
429 significantly stronger ERF_{aci} that exceeded the uncertainty range of the IPCC AR5 and canceled out much of the
430 warming trend of the last century. The conflict between process representation and ERF_{aci} predictions in Jing et al.
431 (2019) underscore a challenge with process-based constraints: improving the representation of a process can result in
432 adverse outcomes to climate prediction due to compensating biases in the model. This challenge is particularly
433 troublesome for constraints on processes like autoconversion that affect the base cloud state because decreasing
434 autoconversion rates can increase total cloud amount, which can yield stronger ERF_{aci}. Thus, a decreased
435 autoconversion rate may improve precipitation outcomes in an ESM that presents the common “too frequent” warm
436 rain bias (e.g., Stephens et al., 2010), yet cause improbably strong ERF_{aci}. Our results show, however, that decreased
437 autoconversion rates result in weaker ERF_{aci_{SW}_SLWCs} (Fig. 3), demonstrating that the base cloud state issue presented
438 in prior studies of autoconversion is not a dominant factor contributing to the ERF_{aci_{SW}} of warm rain processes in
439 E3SMv2.

440 Figure 5a shows the linear relationship between ERF_{aci_{SW}_SLWCs} normalized by the PI SW Cloud Radiative Effect
441 (SWCRE), which represents the fraction of ERF_{aci} that is independent of base cloud state changes, and CFODD slope.
442 The correlation coefficient in Fig. 5a (Pearson’s R = 0.74) is decreased compared to Fig. 3 (Pearson’s R = -0.91).
443 However, comparing the negative correlations between CFODD slope and PI SLWC cloud fraction (Fig. 5b; Pearson’s
444 R = -0.64) and LWP (Fig. 5c; Pearson’s R = -0.89) with Fig. 3, the ERF_{aci_{SW}_SLWCs} increases in magnitude as LWP
445 and cloud fraction decrease, further demonstrating that the contribution of base cloud state to ERF_{aci_{SW}_SLWCs} is
446 relatively minor. The decreased correlation coefficient in Fig. 5a could also be influenced by poor sampling statistics
447 in the “acoef100x” experiment. The acoef100x was the only one of six experiments involving perturbations of the “A”
448 coefficient in KK2000 (Table 1; Sect. 2.4) in which the CFODD slope did not increase with an increase in magnitude
449 of the “A” coefficient. Given the significant decrease in SLWC cloud fraction in this experiment compared to the
450 others (Fig. 5b, Table S2), the CFODD slope result may be affected by insufficient sample size, an additional

451 uncertainty of the CFODD linear regression that is not reflected in the bootstrapping-based uncertainty estimate (Sect.
 452 2).



453
 454 **Figure 5.** Linear regression between (a) E3SMv2 ERFaci_{SW} SLWCs normalized by SWCRE, (b) SLWC cloud fraction, (c) SLWC
 455 LWP and CFODD slopes in 12 PD autoconversion and accretion sensitivity experiments, calculated for SLWCs with MODIS R_e
 456 between 5 and 18 μm . ERFaci_{SW} SLWCs values reflect the SLWCs represented in the corresponding CFODD (i.e., with R_e
 457 corresponding to $5 < R_e < 18 \mu\text{m}$). Error bars represent 1-sigma error estimated from RANSAC-fit bootstrapping (Sect. 2). Grey
 458 and pink shaded regions indicate the 68 and 95% confidence intervals for the MODIS-CloudSat CFODD slope, respectively. Labels
 459 indicate the sensitivity experiment names (Table 1).

460 While we derive a constraint for ERFaci_{SW} using the combined small and medium R_e CFODDs, when the R_e subsets
 461 are considered individually, they show distinct contributions to ERFaci_{SW} SLWCs. Fig. S7 shows that SLWCs with small
 462 R_e have a negative ERFaci_{SW} SLWCs, but that SLWCs in the medium and large R_e subsets have positive ERFaci_{SW} SLWCs
 463 values. This indicates that the dominant effect of aerosols on shortwave radiative forcing in the medium and large
 464 SLWC subsets is decreased cloud fraction, which is reflected in the decreased SLWC sample sizes in the PD
 465 simulations compared to PI (Fig. S8, S9). The negative linear relationship between ERFaci_{SW} SLWCs and CFODD slope
 466 in the medium and large R_e subsets indicates that increasing droplet collection efficiency partially counteracts the
 467 decrease in cloud fraction due to aerosol. The small R_e SLWCs, however, show a positive correlation between
 468 ERFaci_{SW} and CFODD slope, indicating that ERFaci_{SW} weakens as autoconversion rates increase, likely due to
 469 decreased precipitation suppression susceptibility in this subset-subset. The combined small and medium CFODD and
 470 ERFaci_{SW} SLWCs, therefore, represent the convolution of two populations with differing ERFaci_{SW} sensitivities to
 471 autoconversion perturbations. We chose to constrain ERFaci_{SW} using the combined small and medium CFODD and
 472 ERFaci_{SW} SLWCs due to the correlation performance and the dearth of large R_e SLWCs in E3SMv2. However, constraints
 473 for ERFaci_{SW} could potentially be derived for each individual R_e subset or various combinations thereof, depending
 474 on the distribution of SLWCs among the R_e size bins and their contribution to the host model's ERFaci. Considering

475 that constrained $ERF_{\text{Fac}_{\text{SW}}}$ increases in magnitude with increasing R_e in Fig. S7, ~~that the shortwave component of~~
476 ~~ERF_{Fac} is significantly larger than the longwave in CMIP6 models (Smith et al., 2020), and that E3SMv2's total~~
477 ~~ERF_{Fac} (-1.50 W m^{-2}) is relatively strong compared to the IPCC AR6 'very likely' range ($-1.0 \pm 0.7 \text{ W m}^{-2}$) (Forster~~
478 ~~et al., 2021), the underrepresentation of SLWCs with large R_e in E3SMv2 represents a compensating bias, without~~
479 which the total ERF_{Fac} ~~bias~~ would be even ~~larger-stronger~~ compared to IPCC AR6.

Formatted: Superscript

Formatted: Superscript

480 4.2 Limitations of CFODD-based constraint on ERF_{Fac}

481 There are multiple limitations to the CFODD analysis that should be considered in its application as a constraint for
482 ERF_{Fac} . First, droplet collection is not explicitly represented in ESMs with bulk microphysical schemes such as
483 E3SMv2, but is instead implicit in an amalgamation of process and drop size distribution parameterizations controlling
484 the evolution of the cloud and precipitation. Delving into the impact of these individual processes on CFODD-based
485 constraint of ERF_{Fac} is a good target of future work, while autoconversion modulation of ERF_{Fac} was the primary
486 focus here. Furthermore, simulated radar reflectivity is highly sensitive to particle size distribution assumptions in the
487 forward simulator (e.g., Bodas-Salcedo et al., 2011; J. Wang et al., 2021). The host model, therefore, could represent
488 warm rain microphysical processes with high fidelity but still produce biased CFODD profiles when compared with
489 observations. In COSPv2.0, the CloudSat simulator calculates size distributions from an assumed distribution (e.g.,
490 log-normal, gamma, exponential) as well as mass-mixing ratios, precipitation fluxes, and gridbox-mean R_e from the
491 host model. Default COSPv2.0 size distributions were used in this study: log-normal for large-scale stratiform and
492 convective cloud liquid, and exponential for large-scale stratiform and convective cloud rain. The CFODD analysis
493 itself is subject to multiple uncertainties, including the use of simple adiabatic and condensational growth assumptions
494 to scale MODIS COT to ICOD. These assumptions result in a vertical distribution of optical depth, mass
495 concentrations and particle size that may not reflect reality. For example, in the CFODD, particle size and mass
496 concentration are assumed to monotonically increase with height, yet in the real cloud, particle sizes may decrease
497 near the cloud top due to evaporation and entrainment (Suzuki et al., 2010). The uncertainties from assumed
498 hydrometeor size distributions and CFODD construction should be carefully considered when using the CFODD to
499 evaluate model droplet collection efficiencies against observations and in the application as an ERF_{Fac} constraint.
500 Simulated reflectivity biases affect the evaluation of the model CFODD slope against the observational CFODD slope
501 and thus affect the estimation of ERF_{Fac} bias.

502 A few additional limitations on CFODD analysis are imposed by biases in E3SMv2 SLWC representation. The ERFaci
503 constraint is restricted to the small and medium R_e CFODDs because of the underrepresentation of SLWCs with large
504 R_e . SLWCs with medium R_e are also underrepresented in E3SMv2, further limiting the CFODD analysis of E3SMv2
505 ERFaci because process perturbations are limited to the extent that they do not significantly reduce the number of
506 SLWCs with medium R_e . The high reflectivity near cloud top at $ICOD < 4$ in E3SMv2 CFODDs presents another
507 limitation. SLWCs with $COT < 4$ represent a significant fraction of the SLWC population in both A-Train and
508 E3SMv2 (Fig. 2), so including optically thin SLWCs in the linear regression would likely affect the CFODD slope
509 and droplet collection efficiency estimates.

510 Despite these limitations and the uncertainty associated with estimates of droplet collection efficiency from simulated
511 radar reflectivity, CFODD analysis offers a highly desired process-oriented constraint on ERFaci due to warm rain
512 processes. In E3SMv2, the CFODD slope exhibits the expected behavior in response to autoconversion perturbations:
513 slope increases with perturbations that increase the autoconversion rate and decreases with perturbations that decrease
514 the autoconversion rate. Our results also show that the model ERFaci_{sw} is highly sensitive to the processes that the
515 CFODD represents, enabling the constraint of ERFaci_{sw} against the CFODD slope derived from MODIS-CloudSat
516 cloud retrievals. Prior studies have demonstrated that radar reflectivity biases can be partially mitigated by bringing
517 the forward simulator into better agreement with the host model's microphysics parameterization and subgrid
518 variability (Song et al., 2018b; J. Wang et al., 2021). Modified versions of COSP featuring improved consistency with
519 E3SM are to be implemented in future E3SM model versions, which will decrease the uncertainties associated with
520 CFODD analysis of E3SM.

521 5 Summary

522 In this study, we present an updated CFODD analysis and demonstrate how it can be applied to ESMs as a process-
523 oriented constraint on ERFaci. ~~and find that When E3SMv2's CFODD slope is constrained by MODIS-CloudSat~~
524 ~~retrievals, E3SMv2's ERFaci_{sw} agrees with the MODIS-CloudSat constrained value within uncertainty is reduced by~~
525 ~~$14 \pm 6\%$.~~ Demonstrated here as a constraint on the component of ERFaci_{sw} that is modulated by autoconversion,
526 CFODD analysis represents a highly desirable constraint on a process, circumventing the equifinality issue that
527 bedevils atmospheric state variable-based approaches (Mülmenstädt et al., 2020). Limitations of CFODD-based
528 constraint of ERFaci include the implicit representation of droplet collection efficiency in many ESMs, including

529 E3SMv2, the sensitivity of simulated radar reflectivity to droplet size distribution representations and simplifying
530 assumptions applied to construct the CFODD (e.g., adiabatic-condensational growth). While this study focuses on
531 autoconversion, future studies should apply CFODD analysis to other microphysical processes that affect droplet
532 collection efficiency (e.g., accretion, droplet breakup, evaporation) to generate additional ERFaci constraints.

533 Several updates to the WRDs package in COSPv2.0 were made to support the application of CFODD analysis to
534 ESMs. In addition to the original WRDs diagnostics featuring relative frequencies of SLWCs by precipitation intensity
535 and the CFODD by R_e , we have implemented additional diagnostics in the WRDs that include all-sky SLWC
536 frequency maps and MODIS SLWC COT distributions for CFODD sampling statistics. Other updates include the
537 estimation of CFODD slopes using Random Sample Consensus robust linear regression and changes to the SLWC
538 detection schemes for better comparison between observations and satellite simulators.

539 In addition to the modifications of the WRDs described above, the MODIS and CloudSat observational reference data
540 has been updated for consistency with COSPv2.0 SLWC detection. SLWC detection is increased 5-fold in the updated
541 reference data. The increase in SLWC sampling also significantly affected the CFODD distributions and consequently,
542 the A-Train reference droplet collection efficiency at large R_e ($18 \mu\text{m} \leq R_e < 30 \mu\text{m}$). The updated WRDs showed that
543 droplet collection efficiencies in E3SMv2 are decreased compared to observations and SLWCs with small MODIS R_e
544 ($5 \mu\text{m} \geq R_e > 12 \mu\text{m}$) are overrepresented. The E3SMv2 CFODD results also show reflectivities exceeding 0 dBZ near
545 cloud top at $2 < \text{ICOD} < 4$ yet relatively low reflectivities at $\text{ICOD} > 5$. The unreasonably high reflectivities near cloud
546 top may indicate artifacts due to inconsistencies between E3SMv2 outputs and COSPv2.0 inputs to the CloudSat
547 simulator. This issue motivates further investigation in future studies involving applications of the CloudSat simulator
548 to E3SM. The updates described herein have increased the WRDs' utility for evaluating model warm rain process
549 representation and support the analysis needed to derive a constraint on ERFaci from CFODD analysis. Through an
550 evaluation of E3SMv2, we demonstrate that the updated WRDs illuminate specific biases in SLWC representation
551 and provide contextual sampling statistics that are critical for interpreting CFODD results and thus, for future
552 applications of this observational constraint on ERFaci.

553

554 *Code and Data Availability:* The CloudSat and MODIS data products are available from the CloudSat Data Processing
555 Center at CIRA/Colorado State University (<https://www.cloudsat.cira.colostate.edu/>; last access: June 28, 2023). The

556 reference A-Train data used in this study is available here: <https://doi.org/10.5281/zenodo.8384180>. The modified
557 source code of COSPv2.0 is available here: <https://doi.org/10.5281/zenodo.8371120> and the E3SMv2 source code is
558 available here: <https://github.com/E3SM-Project/E3SM> (last access: September 27, 2023). The python package for
559 the two-dimensional Kolmogorov-Smirnov test applied in this study is available here
560 (<https://github.com/svrte/ndtest/tree/master>; last access: June 28, 2023). The python package scikit-learn was used for
561 robust linear regression analysis (<https://scikit-learn.org/stable/>; last access: June 28, 2023).

562 *Author contributions:* CMB led the project, developed the additional WRDs diagnostics in this study, performed the
563 model simulations and wrote the manuscript. PLM provided critical project guidance and support for modeling and
564 analysis. MWC led the A-Train observations analysis and provided guidance on additional WRDs diagnostics
565 development. AV provided input on CFODD analysis applications. JM provided guidance on ERFaci analysis. TM
566 and KS provided guidance on WRDs applications. All authors contributed to writing the manuscript.

567 *Competing Interests:* At least one of the (co-)authors is a member of the editorial board of Atmospheric Chemistry
568 and Physics.

569 *Acknowledgements:* We would like to thank the anonymous reviewers for the thoughtful discussion and insightful
570 feedback. The study was supported as part of the Enabling Aerosol–cloud interactions at GLocal convection-
571 permitting scales (EAGLES) project (project no. 74358) sponsored by the United States Department of Energy
572 (DOE), Office of Science, Office of Biological and Environmental Research (BER), Earth System Model
573 Development (ESMD) program area. The Pacific Northwest National Laboratory (PNNL) is operated for the DOE by
574 the Battelle Memorial Institute under Contract DE-AC05-76RL01830. The research used high-performance
575 computing resources from the PNNL Research Computing, the BER Earth System Modeling program's Compy
576 computing cluster located at PNNL, and resources of the National Energy Research Scientific Computing Center
577 (NERSC), a U.S. Department of Energy Office of Science User Facility located at Lawrence Berkeley National
578 Laboratory, operated under Contract No. DE-AC02-05CH11231, using NERSC awards ALCC-ERCAP0025938 and
579 BER-ERCAP0024471.

580 *Financial support.* This study was funded by the U.S. Department of Energy, Office of Science, Office of Biological
581 and Environmental research, Earth System Model Development (ESMD) program area (project nos. 74358). KS and
582 TM were supported by the Japan Society for the Promotion of Science KAKENHI (Grant JP19H05669), MEXT

583 program for the Advanced Studies of Climate Change Projection (SENTAN) (Grant JPMXD0722680395), and the
584 Environment Research and Technology Development Fund (S-20) (Grant JPMEERF21S12004) of the Environmental
585 Restoration and Conservation Agency. TM was supported by the JST FOREST Program (Grant JPMJFR206Y),
586 and the Japan Society for the Promotion of Science KAKENHI (Grant JP 23K13171).

587

588

589 References

590 Albrecht, B. A.: Aerosols, Cloud Microphysics, and Fractional Cloudiness, *Science*, 245, 1227–1230, pmid =
591 17747885, 10.1126/science.245.4923.1227, 1989.

592

593 Bellouin, N., Quaas, J., Gryspeerdt, E., Kinne, S., Stier, P., Watson-Parris, D., Boucher, O., Carslaw, K. S.,
594 Christensen, M., Daniau, A.-L., Dufresne, J.-L., Feingold, G., Fiedler, S., Forster, P., Gettelman, A.,
595 Haywood, J. M., Lohmann, U., Malavelle, F., Mauritsen, T., ... Stevens, B.: Bounding Global Aerosol
596 Radiative Forcing of Climate Change. *Rev. Geophys.*, 58(1), e2019RG000660,
597 <https://doi.org/https://doi.org/10.1029/2019RG000660>, 2020.

598 Bogenschutz, P. A., Gettelman, A., Morrison, H., Larson, V. E., Craig, C., & Schanen, D. P.: Higher-Order
599 Turbulence Closure and Its Impact on Climate Simulations in the Community Atmosphere Model. *J. Climate*,
600 26(23), 9655–9676 <https://doi.org/https://doi.org/10.1175/JCLI-D-13-00075.1>, 2013.

601 Cesana, G., & Chepfer, H.: How well do climate models simulate cloud vertical structure? A comparison between
602 CALIPSO-GOCCP satellite observations and CMIP5 models. *Geophys. Res. Lett.*, 39(20).
603 <https://doi.org/https://doi.org/10.1029/2012GL053153>, 2012.

604 Christensen, M. W., Stephens, G. L., & Lebsock, M. D.: Exposing biases in retrieved low cloud properties from
605 CloudSat: A guide for evaluating observations and climate data: *J. Geophys. Res.*, 118(21), 12, 112–120, 131.
606 <https://doi.org/https://doi.org/10.1002/2013JD020224>, 2013.

607

608 Dee, D. P., Uppala, S. M., Simmons, A. J., Berrisford, P., Poli, P., Kobayashi, S., Andrae, U., Balmaseda, M. A.,
609 Balsamo, G., Bauer, P., Bechtold, P., Beljaars, A. C. M., van de Berg, L., Bidlot, J., Bormann, N., Delsol, C.,
610 Dragani, R., Fuentes, M., Geer, A. J., Haimberger, L., Healy, S. B., Hersbach, H., Hólm, E. V., Isaksen, L.,
611 Källberg, P., Köhler, M., Matricardi, M., McNally, A. P., Monge-Sanz, B. M., Morcrette, J.-J., Park, B.-K.,
612 Peubey, C., de Rosnay, P., Tavolato, C., Thépaut, J.-N., and Vitart, F.: The ERA-Interim reanalysis:
613 configuration and performance of the data assimilation system, *Quarterly Journal of the Royal Meteorological*
614 *Society*, 137, 553–597, <https://doi.org/10.1002/qj.828>, 2011.

615

616 Gelaro, R., McCarty, W., Suárez, M. J., Todling, R., Molod, A., Takacs, L., Randles, C. A., Darmenov, A.,
617 Bosilovich, M. G., Reichle, R., Wargan, K., Coy, L., Cullather, R., Draper, C., Akella, S., Buchard, V.,
618 Conaty, A., da Silva, A. M., Gu, W., ... Zhao, B.: The Modern-Era Retrospective Analysis for Research and
619 Applications, Version 2 (MERRA-2), *Journal of Climate*, 30(14), 5419–5454, <https://doi.org/10.1175/JCLI-D-16-0758.1>, 2017.

620

621 Ghan, S. J.: Technical Note: Estimating aerosol effects on cloud radiative forcing, *Atmospheric Chemistry and*
622 *Physics*, 13(19), 9971–9974. <https://doi.org/10.5194/acp-13-9971-2013>, 2013.

623 Golaz, J. C., Larson, V. E., & Cotton, W. R.: A PDF-based model for boundary layer clouds. Part I: Method and
624 model description, *Journal of the Atmospheric Sciences*, 59(24), 3540–3551. [https://doi.org/10.1175/1520-0469\(2002\)059<3540:APBMFB>2.0.CO;2](https://doi.org/10.1175/1520-0469(2002)059<3540:APBMFB>2.0.CO;2), 2022.

626 Golaz, J.-C., Van Roekel, L. P., Zheng, X., Roberts, A. F., Wolfe, J. D., Lin, W., Bradley, A. M., Tang, Q., Maltrud,
627 M. E., Forsyth, R. M., Zhang, C., Zhou, T., Zhang, K., Zender, C. S., Wu, M., Wang, H., Turner, A. K., Singh,
628 B., Richter, J. H., ... Bader, D. C.: The DOE E3SM Model Version 2: Overview of the Physical Model and
629 Initial Model Evaluation. *Journal of Advances in Modeling Earth Systems*, 14(12), e2022MS003156.
630 <https://doi.org/https://doi.org/10.1029/2022MS003156>, 2022.

631 Jing, X., Suzuki, K., Guo, H., Goto, D., Ogura, T., Koshiro, T., and Mülmenstädt, J.: A Multimodel Study on Warm
632 Precipitation Biases in Global Models Compared to Satellite Observations, *Journal of Geophysical Research: Atmospheres*, 122, 11, 806-811, 824, <https://doi.org/10.1002/2017JD027310>, issue = 21, 2017.

634
635 Jing, X., Suzuki, K., & Michibata, T.: The Key Role of Warm Rain Parameterization in Determining the Aerosol
636 Indirect Effect in a Global Climate Model. *Journal of Climate*, 32(14), 4409–4430.
637 <https://doi.org/https://doi.org/10.1175/JCLI-D-18-0789.1>, 2019.

638 Kay, J. E., Wall, C., Yettella, V., Medeiros, B., Hannay, C., Caldwell, P., & Bitz, C.: Global climate impacts of
639 fixing the Southern Ocean shortwave radiation bias in the Community Earth System Model (CESM), *Journal
640 of Climate*, 29(12), 4617–4636. <https://doi.org/10.1175/JCLI-D-15-0358.1>, 2016.

641 Khairoutdinov, M., & Kogan, Y. (2000). A New Cloud Physics Parameterization in a Large-Eddy Simulation Model
642 of Marine Stratocumulus. *Monthly Weather Review*, 128(1), 229–243.
643 [https://doi.org/https://doi.org/10.1175/1520-0493\(2000\)128<0229:ANCPPI>2.0.CO;2](https://doi.org/https://doi.org/10.1175/1520-0493(2000)128<0229:ANCPPI>2.0.CO;2)

644 Kogan, Y.: A Cumulus Cloud Microphysics Parameterization for Cloud-Resolving Models, *Journal of the
645 Atmospheric Sciences*, 70, 1423-1436, <https://doi.org/10.1175/JAS-D-12-0183.1>, 2013.

646
647 Larson, V. E.: CLUBB-SILHS: A parameterization of subgrid variability in the atmosphere,
648 <http://arxiv.org/abs/1711.03675>, 2017.

649 Larson, V. E., & Golaz, J.-C.: Using Probability Density Functions to Derive Consistent Closure Relationships
650 among Higher-Order Moments. *Monthly Weather Review*, 133(4), 1023–1042.
651 <https://doi.org/https://doi.org/10.1175/MWR2902.1>, 2005.

652 Liu, X., Easter, R. C., Ghan, S. J., Zaveri, R., Rasch, P., Shi, X., Lamarque, J. F., Gettelman, A., Morrison, H., Vitt,
653 F., Conley, A., Park, S., Neale, R., Hannay, C., Ekman, A. M. L., Hess, P., Mahowald, N., Collins, W.,
654 Iacono, M. J., ... Mitchell, D.: Toward a minimal representation of aerosols in climate models: Description
655 and evaluation in the Community Atmosphere Model CAM5. *Geoscientific Model Development*, 5(3), 709–
656 739. <https://doi.org/10.5194/GMD-5-709-2012>, 2012.

657 Liu, X., Ma, P.-L., Wang, H., Tilmes, S., Singh, B., Easter, R. C., Ghan, S. J., & Rasch, P. J. Description and
658 evaluation of a new four-mode version of the Modal Aerosol Module (MAM4) within version 5.3 of the
659 Community Atmosphere Model. *Geoscientific Model Development*, 9(2), 505–522,
660 <https://doi.org/10.5194/gmd-9-505-2016>, 2016.

661 Mangla, R., Indu, J., & Lakshmi, V.: Evaluation of convective storms using spaceborne radars over the Indo-
662 Gangetic Plains and western coast of India. *Meteorological Applications*, 27(3), e1917,
663 <https://doi.org/https://doi.org/10.1002/met.1917>, 2020.

664 Marchand, R., Mace, G. G., Ackerman, T., & Stephens, G.: Hydrometeor Detection Using Cloudsat—An Earth-
665 Orbiting 94-GHz Cloud Radar, *Journal of Atmospheric and Oceanic Technology*, 25(4), 519–533,
666 <https://doi.org/10.1175/2007JTECHA1006.1>, 2008.

667 Michibata, T., Kawamoto, K., & Takemura, T.: The effects of aerosols on water cloud microphysics
668 and macrophysics based on satellite-retrieved data over East Asia and the North Pacific, *Atmospheric*
669 *Chemistry and Physics*, 14(21), 11935–11948, <https://doi.org/10.5194/acp-14-11935-2014>, 2014.

670 Michibata, T., Suzuki, K., Ogura, T., & Jing, X.: Data for the publication “Incorporation of inline warm rain
671 diagnostics into the COSP2 satellite simulator for process-oriented model evaluation.” Zenodo,
672 <https://doi.org/10.5281/zenodo.3370823>, 2019a.

673 Michibata, T., Suzuki, K., Ogura, T., & Jing, X.: Incorporation of inline warm rain diagnostics into the COSP2
674 satellite simulator for process-oriented model evaluation. *Geoscientific Model Development*, 12(10), 4297–
675 4307. <https://doi.org/10.5194/gmd-12-4297-2019>, 2019b.

676 Muhlbauer, A., McCoy, I. L., and Wood, R.: Climatology of stratocumulus cloud morphologies: Microphysical
677 properties and radiative effects, *Atmos. Chem. Phys.*, 14, 2014.
678

679 Mülmenstädt, J. and Feingold, G.: The Radiative Forcing of Aerosol–Cloud Interactions in Liquid Clouds: Wrestling
680 and Embracing Uncertainty, *Current Climate Change Reports*, 4, 23-40, 10.1007/s40641-018-0089-y, 2018.
681

682 Mülmenstädt, J., Nam, C., Salzmann, M., Kretschmar, J., L'Ecuyer, T. S., Lohmann, U., Ma, P.-L., Myhre, G.,
683 Neubauer, D., Stier, P., Suzuki, K., Wang, M., & Quaas, J. (2020). Reducing the aerosol forcing uncertainty
684 using observational constraints on warm rain processes. *Science Advances*, 6(22), eaaz6433.
685 <https://doi.org/10.1126/sciadv.aaz6433>

686 Partain, P., & Cronk, H.: *CloudSat ECMWF-AUX auxiliary data product process description and interface control*
687 *document*. California Institute of Technology Jet Propulsion Laboratory Doc., 15 pp.,
688 [https://www.cloudsat.cira.colostate.edu/cloudsat-static/info/dl/ecmwf-aux/ECMWF-](https://www.cloudsat.cira.colostate.edu/cloudsat-static/info/dl/ecmwf-aux/ECMWF-AUX_PDICD.P_R05.rev0_.pdf)
689 [AUX_PDICD.P_R05.rev0_.pdf](https://www.cloudsat.cira.colostate.edu/cloudsat-static/info/dl/ecmwf-aux/ECMWF-AUX_PDICD.P_R05.rev0_.pdf), 2017, last access: 24 January 2024.

690 Platnick, S., Meyer, K. G., King, M. D., Wind, G., Amarasinghe, N., Marchant, B., Arnold, G. T., Zhang, Z.,
691 Hubanks, P. A., Holz, R. E., Yang, P., Ridgway, W. L., & Riedi, J.: The MODIS Cloud Optical and
692 Microphysical Products: Collection 6 Updates and Examples From Terra and Aqua. *IEEE Transactions on*
693 *Geoscience and Remote Sensing*, 55(1), 502–525, <https://doi.org/10.1109/TGRS.2016.2610522>, 2017.

694 Rasch, P. J., Xie, S., Ma, P. L., Lin, W., Wang, H., Tang, Q., Burrows, S. M., Caldwell, P., Zhang, K., Easter, R. C.,
695 Cameron-Smith, P., Singh, B., Wan, H., Golaz, J. C., Harrop, B. E., Roesler, E., Bacmeister, J., Larson, V. E.,
696 Evans, K. J., ... Yang, Y.: An Overview of the Atmospheric Component of the Energy Exascale Earth System
697 Model: *Journal of Advances in Modeling Earth Systems*, 11(8), 2377–2411.
698 <https://doi.org/10.1029/2019MS001629>, 2019.

699 Sato, Y., Goto, D., Michibata, T., Suzuki, K., Takemura, T., Tomita, H., and Nakajima, T.: Aerosol effects on cloud
700 water amounts were successfully simulated by a global cloud-system resolving model, *Nature Communications*,
701 9, 985, 10.1038/s41467-018-03379-6, 2018.
702

703 Smith, C. J., Kramer, R. J., Myhre, G., Alterskjær, K., Collins, W., Sima, A., Boucher, O., Dufresne, J.-L., Nabat, P.,
704 Michou, M., Yukimoto, S., Cole, J., Paynter, D., Shioyama, H., O'Connor, F. M., Robertson, E., Wiltshire, A.,
705 Andrews, T., Hannay, C., Miller, R., Nazarenko, L., Kirkevåg, A., Olivieri, D., Fiedler, S., Lewinschal, A.,
706 Mackallah, C., Dix, M., Pincus, R., & Forster, P.: Effective radiative forcing and adjustments in CMIP6 models,
707 *Atmospheric Chemistry and Physics*, 20, 9591–9618, 10.5194/acp-20-9591-2020, 2020.
708

709 Song, H., Zhang, Z., Ma, P.-L., Ghan, S. J., & Wang, M.: An Evaluation of Marine Boundary Layer Cloud Property
710 Simulations in the Community Atmosphere Model Using Satellite Observations: Conventional Subgrid
711 Parameterization versus CLUBB. *Journal of Climate*, 31(6), 2299–2320,
712 <https://doi.org/https://doi.org/10.1175/JCLI-D-17-0277.1>, 2018a.

713 Song, H., Zhang, Z., Ma, P.-L., Ghan, S., & Wang, M.: The importance of considering sub-grid cloud variability
714 when using satellite observations to evaluate the cloud and precipitation simulations in climate models.
715 *Geoscientific Model Development*, 11(8), 3147–3158. <https://doi.org/10.5194/gmd-11-3147-2018>, 2018b.

716 Stephens, G. L., L'Ecuyer, T., Forbes, R., Gettelmen, A., Golaz, J.-C., Bodas-Salcedo, A., Suzuki, K., Gabriel, P., &
717 Haynes, J.: Dreary state of precipitation in global models. *Journal of Geophysical Research: Atmospheres*,
718 115(D24), <https://doi.org/https://doi.org/10.1029/2010JD014532>, 2010.

719 Stevens, B. and Feingold, G.: Untangling aerosol effects on clouds and precipitation in a buffered system, *Nature*,
720 461, 607–613, 10.1038/nature08281, 2009.
721

722 Suzuki, K., Nakajima, T. Y., & Stephens, G. L.: Particle Growth and Drop Collection Efficiency of Warm Clouds as
723 Inferred from Joint CloudSat and MODIS Observations. *Journal of the Atmospheric Sciences*, 67(9), 3019–
724 3032, <https://doi.org/10.1175/2010JAS3463.1>, 2010.

725 Suzuki, K., Stephens, G., Bodas-Salcedo, A., Wang, M., Golaz, J.-C., Yokohata, T., & Koshiro, T.: Evaluation of
726 the Warm Rain Formation Process in Global Models with Satellite Observations. *Journal of the Atmospheric
727 Sciences*, 72(10), 3996–4014, <https://doi.org/https://doi.org/10.1175/JAS-D-14-0265.1>, 2015.

728 Suzuki, K., Stephens, G. L., & Lebsack, M. D.: Aerosol effect on the warm rain formation process: Satellite
729 observations and modeling. *Journal of Geophysical Research: Atmospheres*, 118(1), 170–184,
730 <https://doi.org/https://doi.org/10.1002/jgrd.50043>, 2013.

731 Takahashi, H., Bodas-Salcedo, A., and Stephens, G.: Warm Cloud Evolution, Precipitation, and Their Weak Linkage
732 in HadGEM3: New Process-Level Diagnostics Using A-Train Observations, *Journal of the Atmospheric
733 Sciences*, 78, 2075–2087, <https://doi.org/10.1175/JAS-D-20-0321.1>, 2021.

734 Wang, H., Easter, R. C., Zhang, R., Ma, P. L., Singh, B., Zhang, K., Ganguly, D., Rasch, P. J., Burrows, S. M.,
735 Ghan, S. J., Lou, S., Qian, Y., Yang, Y., Feng, Y., Flanner, M., Leung, R. L., Liu, X., Shrivastava, M., Sun,
736 J., ... Yoon, J. H.: Aerosols in the E3SM Version 1: New Developments and Their Impacts on Radiative
737 Forcing. *Journal of Advances in Modeling Earth Systems*, 12(1), <https://doi.org/10.1029/2019MS001851>,
738 2020.

739 Wang, J., Fan, J., Houze, R. A., Brodzik, S. R., Zhang, K., Zhang, G. J., & Ma, P. L.: Using radar observations to
740 evaluate 3-D radar echo structure simulated by the Energy Exascale Earth System Model (E3SM) version 1.
741 *Geoscientific Model Development*, 14(2), 719–734. <https://doi.org/10.5194/gmd-14-719-2021>, 2021.

742 Wood, R.: Drizzle in Stratiform Boundary Layer Clouds. Part II: Microphysical Aspects. *Journal of the Atmospheric
743 Sciences*, 62(9), 3034–3050. <https://doi.org/https://doi.org/10.1175/JAS3530.1>, 2005.

744 Zhang, G. J., & McFarlane, N. A.: Sensitivity of climate simulations to the parameterization of cumulus convection
745 in the Canadian climate centre general circulation model. *Atmosphere-Ocean*, 33(3), 407–446.
746 <https://doi.org/10.1080/07055900.1995.9649539>, 1995.

747 Zhang, M., Xie, S., Liu, X., Lin, W., Zhang, K., Ma, H.-Y., Zheng, X., & Zhang, Y.: Toward Understanding the
748 Simulated Phase Partitioning of Arctic Single-Layer Mixed-Phase Clouds in E3SM. *Earth and Space Science*,
749 7(7), e2020EA001125. <https://doi.org/https://doi.org/10.1029/2020EA001125>, 2020.

750 Zhang, M., Xie, S., Liu, X., Lin, W., Zheng, X., Golaz, J.-C., & Zhang, Y.: Cloud Phase Simulation at High Latitudes
751 in EAMv2: Evaluation Using CALIPSO Observations and Comparison With EAMv1. *Journal of Geophysical
752 Research: Atmospheres*, 127(22), e2022JD037100. <https://doi.org/https://doi.org/10.1029/2022JD037100>,
753 2022.

754 Zhang, Y., Klein, S. A., Boyle, J., & Mace, G. G.: Evaluation of tropical cloud and precipitation statistics of
755 Community Atmosphere Model version 3 using CloudSat and CALIPSO data. *Journal of Geophysical
756 Research: Atmospheres*, 115(D12). <https://doi.org/https://doi.org/10.1029/2009JD012006>, 2010.

757 Zhang, Y., Xie, S., Lin, W., Klein, S. A., Zelinka, M., Ma, P.-L., Rasch, P. J., Qian, Y., Tang, Q., & Ma, H.-Y.:
758 Evaluation of Clouds in Version 1 of the E3SM Atmosphere Model With Satellite Simulators. *Journal of*
759 *Advances in Modeling Earth Systems*, 11(5), 1253–1268,
760 <https://doi.org/https://doi.org/10.1029/2018MS001562>, 2019a.

761 Zhang, Y., Xie, S., Lin, W., Klein, S. A., Zelinka, M., Ma, P.-L., Rasch, P. J., Qian, Y., Tang, Q., & Ma, H.-Y.:
762 Evaluation of Clouds in Version 1 of the E3SM Atmosphere Model With Satellite Simulators. *Journal of*
763 *Advances in Modeling Earth Systems*, 11(5), 1253–1268.
764 <https://doi.org/https://doi.org/10.1029/2018MS001562>, 2019b.

765

766

767

768

769